# STARS

Electronic Theses and Dissertations, 2004-2019

2019

# A Multi-Species Single-LED Hazardous Gas Sensor for Commercial Space Applications

Akshita Parupalli
*University of Central Florida*

# A MULTI-SPECIES SINGLE-LED HAZARDOUS GAS SENSOR FOR

# COMMERCIAL SPACE APPLICATIONS

by

AKSHITA PARUPALLI

B.S. University of Central Florida, 2017

A thesis submitted in partial fulfillment of the requirements
for the degree of Master of Science
in the Department of Mechanical and Aerospace Engineering
in the College of Engineering and Computer Sciences
at the University of Central Florida
Orlando, Florida

Spring Term
2019

Major Professor: Subith Vasu

# ABSTRACT

In the interest of furthering both commercial and government-funded opportunities for deep space exploration, the safety of life and equipment onboard must be absolutely certain. In this regard, the presence of any hazardous gases or combustion events onboard space vehicles must be quickly characterized and detected. Several hazardous gases of interest have absorption features in the mid-infrared range and can be detected with an infrared light source, via the principles of absorption spectroscopy. A non-dispersive infrared (NDIR) sensor that follows these principles has been developed to utilize light-emitting diodes (LEDs) for gas detection and quantification. LEDs contain a particular advantage in this situation because they have low power requirements, are robust and easily adaptable, and they are cheaper than existing laser-based systems. The design has successfully performed several laboratory, environmental chamber, and high-altitude balloon flight tests. The main purpose of these various tests was to place the sensor in challenging environments, examine the effects on sensor performance, and adjust accordingly.

The current sensor design utilizes a single 4.2µm LED and a rotating diffraction grating to detect both carbon dioxide ($CO_2$) and nitrous oxide ($N_2O$) within a single scan. These measurements were further validated using two distributed feedback quantum cascade lasers (QCL) centered at 4.25µm and 4.58µm. The sensor collected data on a wavelength range of 4117nm to 4592nm. Mixtures containing the concentrations of the two species of interest varying from 0.2% to 0.8% were analyzed. The integrated absorbance data was calculated for each species and compared with theoretical predictions. The results show that the data follows the expected behavior and correlates better at lower concentrations. Subsequent work on this sensor will focus on increasing the quantity of identifiable gases and on further testing in hazardous environments.

*To my family: Thank you for the unconditional love and support.*

# ACKNOWLEDGMENTS

I would like to thank my advisor, Dr. Vasu, for giving me the opportunity to get into research. I would also like to thank my committee members, Dr. Ahmed and Dr. Chow.

I would like to thank everyone who has worked on this project both in the past and in the present: Dr. Anthony Terraciano, Kyle Thurmond, Zachary Loparo, Justin Urso, and Michael Villar. I am grateful to all of my lab mates for all of the help and advice that I have received along the way. Their help was instrumental in the completion of this thesis. Thank you to my friends, for the moral support and encouragement you've provided along the way.

# TABLE OF CONTENTS

# LIST OF FIGURES

# LIST OF TABLES

# LIST OF ABBREVIATIONS

| | | |
|---|---|---|
| CO | = | Carbon monoxide |
| $CO_2$ | = | Carbon dioxide |
| COE CST | = | Center of Excellence Commercial Space Transportation |
| DAQ | = | Data Acquisition Unit |
| ECLSS | = | Environmental Control and Life Support System |
| FAA | = | Federal Aviation Administration |
| HASP | = | High Altitude Student Payload |
| LED | = | Light-emitting diode |
| MIR | = | Mid-infrared |
| $N_2$ | = | Nitrogen |
| $N_2O$ | = | Nitrous oxide |
| NASA | = | National |
| NDIR | = | Non-dispersive infrared |
| ORNL | = | Oak Ridge National Laboratories |
| QCL | = | Quantum cascade laser |
| UCF | = | University of Central Florida |

# CHAPTER ONE: INTRODUCTION

Motivation

The basis of this work is to propose the use of light-emitting diodes (LEDs) in order to quickly and robustly detect hazardous gases in low gravity environments. This detection and characterization of hazardous gases is essential for the goal of furthering the possibilities of deep space exploration. In a confined environment, such as aboard a spacecraft, hazardous gas leaks cannot always be quickly diluted or mitigated in the same manner as on Earth. In such a situation, rapid detection is essential for preserving human life onboard. A sensor that utilizes LEDs and the principles of absorption spectroscopy would be able to quickly and accurately quantify the presence of targeted gases within its spectral range, regardless of the challenging environment.

The primary motivation for the creation of this sensor is to satisfy the Federal Aviation Administration Center of Excellence Commercial Space Transportation (FAA COE CST) Research Areas 3.3 and 3.4 in regards to the Environmental Control and Life Support System (ECLSS) and human habitability [1]. With the increasing likelihood that space tourism will develop into a viable industry, the number of launches into space by both the government and commercial enterprises will increase. The FAA and the pioneers in the space tourism industry have expressed an interest in a durable, sensitive sensor that is cost-effective and has low power consumption. Before space tourism can begin bringing crews and consumers into space, the FAA must be assured that all safety standards are met, including the fire detection and suppression systems. In NASA's Technology Roadmaps, under Technology Area 6: Human Health, Life Support, and Habitation Systems, this technology can be utilized as an atmospheric-constituent sensor for primary life support systems used in both fire and hazardous gas detection [2]. These

detection systems should be located at various locations beyond simply the crew cabin location, such as near fuel and oxidizer storage areas, scientific testing areas, and cargo bays; thus, they should also be able to withstand lower pressures and temperatures.

<center>Species of Interest</center>

The primary focus of this sensor has always been the detection of carbon dioxide ($CO_2$), primarily because it is a trace gas that increases in concentration in the event of smoldering or burning materials. Rapid monitoring of $CO_2$ levels allows for enhanced early fire hazard detection in space vehicles. Another common source of $CO_2$ is human respiration, thus fluctuating concentration values could also indicate issues with air quality management within a confined environment [3].

$CO_2$ has absorption features in the mid-infrared range, with peaks of interest located at approximately 4.2 μm. The principles of absorption spectroscopy will be discussed in further detail in Chapter Two, but it is important to mention here because $CO_2$'s absorption features were taken into account when considering other species of interest. One additional species of interest is carbon monoxide (CO), primarily because it is another indicator of total exhaust carbon output. CO is extremely dangerous to humans even when present in low concentrations . CO has absorption features in the 4.7 μm range with minimal interference with $CO_2$. The third species of interest is nitrous oxide ($N_2O$), a common oxidizer used in hybrid rockets such as Virgin Galactic's RocketMotorTwo [4]. $N_2O$ is also a common sedative used in dentistry (also known as "laughing gas") and could therefore impact human cognitive function in the case of a leak. $N_2O$ has features in the 4.5 μm range, and it has minimal interference with $CO_2$ but can be seen to overlap with CO in Figure 1; hence, all tests focus on either CO or $N_2O$ along with $CO_2$, but not both.

<center>2</center>
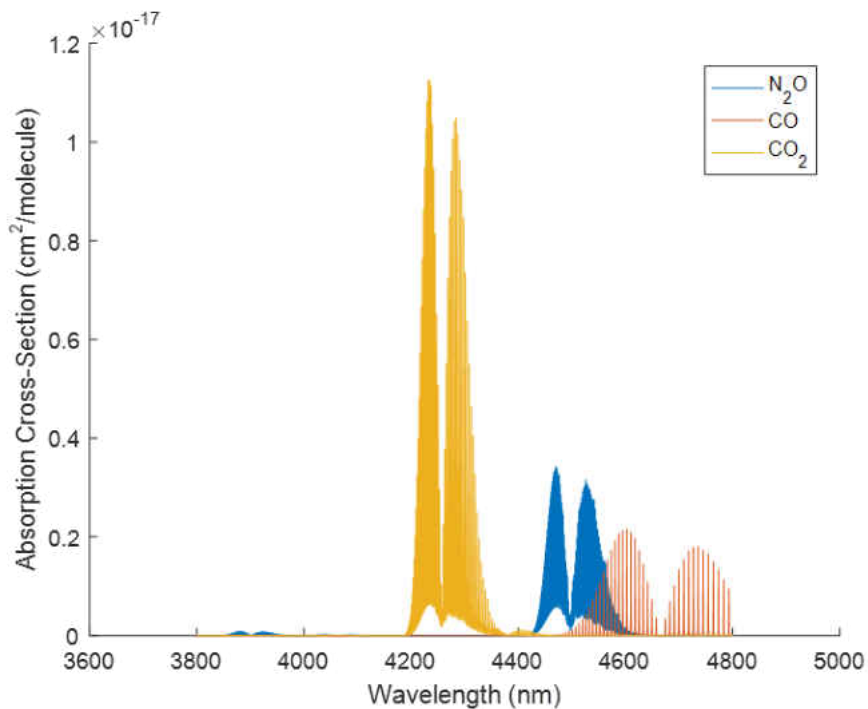
**Figure 1:** Absorption features for $CO_2$, $N_2O$, and CO. This data is taken from the HITRAN database [5].

Current Detection Systems

Fire detection systems are well-established in both commercial and private use on Earth, but these sensors often rely on particle-based detection. This type of detection is generally inappropriate for space applications, because the absence of gravity has a clear effect on the behavior of a combustion reaction; as a result, false positives are particularly common when using particle-based detectors [6]. In addition, these types of sensors are incapable of detecting toxic gases. Additional separate units are often required for each hazardous gas to be measured, such as with CO detectors.

The combustion and hazardous gas sensors that are currently being utilized in space environments primarily rely on laser-based absorption spectroscopy [7, 8]. While this procedure works well both on Earth and in more challenging space environments, lasers are not without

disadvantages. Laser output is susceptible to fluctuations in temperature and pressure; in addition, they are quite expensive and have large power requirements compared to their output intensity. Furthermore, since the output of a laser is spectrally limited, it is normally necessary to have a separate laser for each species to be detected, which further increases operational costs [8].

Light-emitting diodes (LEDs) are proposed for use in absorption-spectroscopy based sensors instead of lasers in this work. The primary advantages of LEDs are that they are inexpensive, more robust, and less demanding in terms of power requirements. LEDs are also a much more spectrally broad source than lasers, which means that a single LED can potentially be used to detect multiple species.

<u>Organization of Thesis</u>

A brief outline of this thesis is presented:

- Chapter Two discusses the necessary theory and background information required to understand the concepts involved. These concepts primarily include the principles of absorption spectroscopy, their use with various light sources, and their implementation with diffraction gratings.

- Chapter Three describes the history of the sensor in question. I have been a part of this project since my undergraduate career at the University of Central Florida, and so a brief description of the initial efforts is introduced. A more in-depth discussion is presented on research that has been performed since beginning a graduate career, including a high-altitude balloon flight.

- Chapter Four presents a detailed discussion of the most current design and its results; this version will be referred to as the "rotating grating design". This design uses a single LED to detect two species of interest within a single test. The use of a rotating diffraction grating allows for the creation of an absorbance curve along a specified wavelength range instead of at a single point. The integrated absorbance is calculated for each species and is compared with a spectrally convolved theoretical prediction. The sensor setup is also validated by comparing the LED data with measurements taken with two distributed feedback quantum cascade lasers (QCLs).

- Chapter Five draws conclusions on the sensor and discusses directions of improvement for the overall design and validation.

# CHAPTER TWO: THEORY

Absorption Spectroscopy

Absorption spectroscopy relies on a gaseous species' particular characteristics of attenuating certain wavelengths of light; if the path length, reference intensity, and environment temperature are known, then concentration measurements can be performed [9]. In species concentration measurement, a collimated beam of light with a wavelength characteristic to the targeted species is directed through a test medium, as shown in Figure 2 below. The attenuation of the beam is measured by comparing the incident and transmitted intensity, which is related to molecular concentration through the Beer-Lambert Law, listed as Equation 1 below. This equation uses the *reference intensity $I_{\lambda,0}$ (W·cm$^{-2}$)* and the *transmitted intensity $I_\lambda$ (W·cm$^{-2}$)* in order to calculate the *spectral absorbance A(λ) (unitless)*. The *concentration of the species of interest*, $n_i$ *(mol/cm$^3$)*, can then be provided that the *wavelength-specific absorption coefficient $\alpha_{\lambda,i}$ (cm$^{-1}$)* and the *path length L (cm)* are known. The absorption coefficient is further defined in Equation 2 and is typically taken from the HITRAN database. $S_\lambda$ *(atm$^{-1}$·cm$^{-2}$)* is the *spectral line strength*, $\phi_\lambda$ *(cm)* is the *line shape function*, and $\chi_i$ *(unitless)* is the *mole fraction of the i$^{th}$ species*. The absorption coefficient is known to vary with temperature, and so the environmental temperature must be closely monitored for any fluctuations [5].

$$A(\lambda) = -ln\left(\frac{I_\lambda}{I_{\lambda,0}}\right) = \alpha_{\lambda,i} n_i L \tag{1}$$

$$\alpha_{\lambda,i} = S_\lambda \cdot \phi_\lambda \cdot \chi_i \tag{2}$$
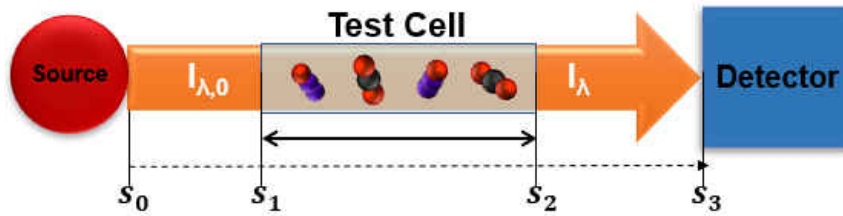
**Figure 2:** Schematic of a typical absorption spectroscopy setup. The test cell contains the species of interest, and light passes from the source to the detector.

Figure 3 shows the varying light intensities at different locations along the path length in the previous figure. The initial reference intensity at the source is depicted as $I_{\lambda,0,s_0}$. The reference intensity at the detector, in the case of zero absorption, is shown as $I_{\lambda,0,s_3}$; the difference between this value and the initial reference intensity represents the loss in signal due to the path length and optical components that may reduce the signal. The transmitted intensity is shown as $I_{\lambda,s_3}$ and depicts absorption occurring due to a species of interest being present in the test cell.
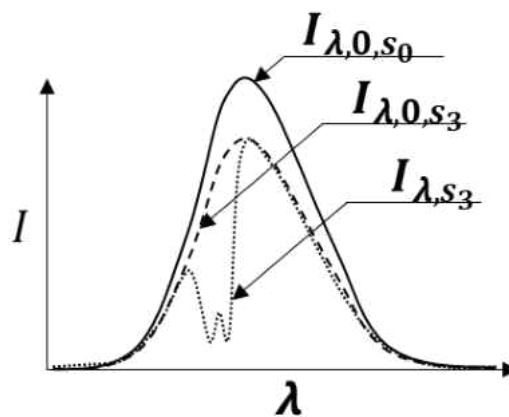


**Figure 3:** Light intensity at various locations along a path length. The figure depicts both the case of no absorption and the case of absorption due to a species of interest being present in the test cell.

7

<u>Reflective Diffraction Gratings</u>

One major advantage of LEDs that is taken into account with the most recent sensor design is the broad spectral output. This means that the LED emits light at a range of wavelengths beyond the peak wavelength. Since this light is from one source, it needs to be separated somehow in order to analyze separate species with characteristics at different wavelengths. This is done via the use of a reflective diffraction grating, which allows for the chromatic separation of the source light [10]. Equation 3 below relates the incident and reflected angles, as depicted in Figure 4, to the wavelength of diffracted light.

$$\boldsymbol{\beta = asin\left(\frac{n \cdot \lambda}{d} - sin(\alpha)\right)} \tag{3}$$

In this equation, **n** represents the *order of diffraction (unitless)*. At the zeroth order, the incident monochromatic light is reflected at the same angle to the normal. At the first order, and all increasing orders thereafter, the light is diffracted to a specific wavelength. The first order is the primarily the only one of concern in this situation, as intensity rapidly decreases as order of diffraction increases. The *wavelength λ (μm)* that will ultimately reach the detector can then be determined, provided that the *grating constant **d** (mm)* and the necessary angles **α** (*incident*) and **β** *(wavelength dependent diffracted angle)* are known. The grating constant corresponds to the size of the reflective features on the gratings surface, as seen in the figure.

Figure 4 below shows how the incident light is diffracted such that a monochromatic order of light leaves at a different orientation than the incident angle. Diffraction gratings are typically used in conjunction with an optical slit in order to prevent accidental measurements of any scattered light.
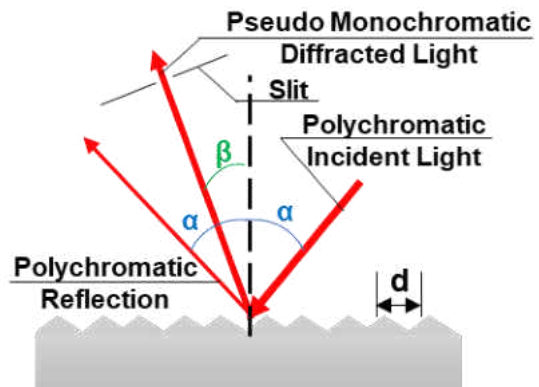
**Figure 4:** Diffraction grating schematic showing the incident light, monochromatic diffracted light, and the reflection of the incident light.

# CHAPTER THREE: SENSOR HISTORY

## Preliminary Benchtop Design

The original design for the sensor was developed by Thurmond et al. in labs at UCF and Oak Ridge National Laboratories (ORNL) and has been evaluated for performance and calibrations; much of the description and results shown here are presented in the ensuing journal paper [11]. This sensor utilized three LEDs: one reference centered at $3.6\mu$m, one centered at $4.2\mu$m for measuring $CO_2$, and one centered at $4.7\mu$m for measuring CO; the schematic is presented in Figure 5. The three LEDs were filtered and collimated separately before being combined through the use of two beam splitters. This light was then transmitted through a test cell containing the gas mixture under investigation, before being focused onto the detector.
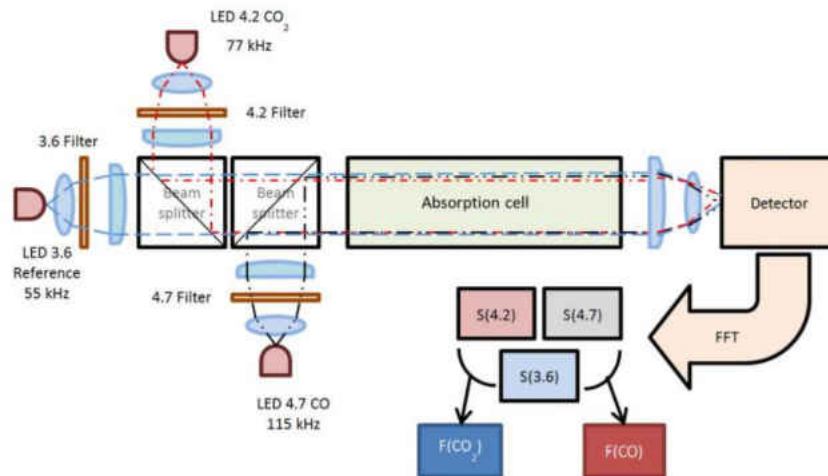


**Figure 5:** Preliminary sensor hardware and processing schematic [11].

Each LED's amplitude was modulated at a different frequency so that the combined signal could easily be separated via Fourier transform. Then, with the use of Equation 1, the concentrations of CO and $CO_2$ present in the test mixture could be determined. Simultaneous measurements of CO and $CO_2$ were performed in order to observe any potential interference

between the species. The signal was well-resolved for fluctuations up to 250 Hz. Time resolution measurements were performed as well in order to demonstrate sensor speed. The sensor was ultimately determined to have detectability limits of 30ppm ($CO_2$) and 400ppm (CO), and no interference between species was observed. The basic benchtop model underwent both laboratory and environmental chamber testing, while an adapted version underwent a high-altitude balloon flight via the High Altitude Student Payload (HASP) program [12].

<u>High-Altitude Balloon Flight</u>

The balloon flight discussed here is the second flight test that this system has undergone, and it is described in more detail because this work occurred during my graduate career at the university. Much of the detail from this section is referenced from the journal publication by Terracciano et al. and the flight report submitted to HASP [13, 14].

*Sensor Design*

This primary goal of this design was to monitor $CO_2$ detection while aboard a high-altitude balloon flight. Only one species was focused on in order to minimize the complexity and size of the overall system. One flight test had already been completed with the original optical schematic designed by Thurmond et al., and this flight test sought to correct some of the challenges presented and further study the effects that the high altitude had on the sensor [11, 12]. Primarily, the focus was the effects of changing temperature and pressure on the setup. Figure 6 shows the predicted absorption cross-section curves for the 4.2 LED (LED42, IoffeLED) at varying temperatures and pressures [15]. Both variables are seen to have an effect on the overall signal; as pressure decreases, the peak width is seen to narrow; additionally, the baseline absorbance decreases. As temperature decreases, the overall absorbance increases.
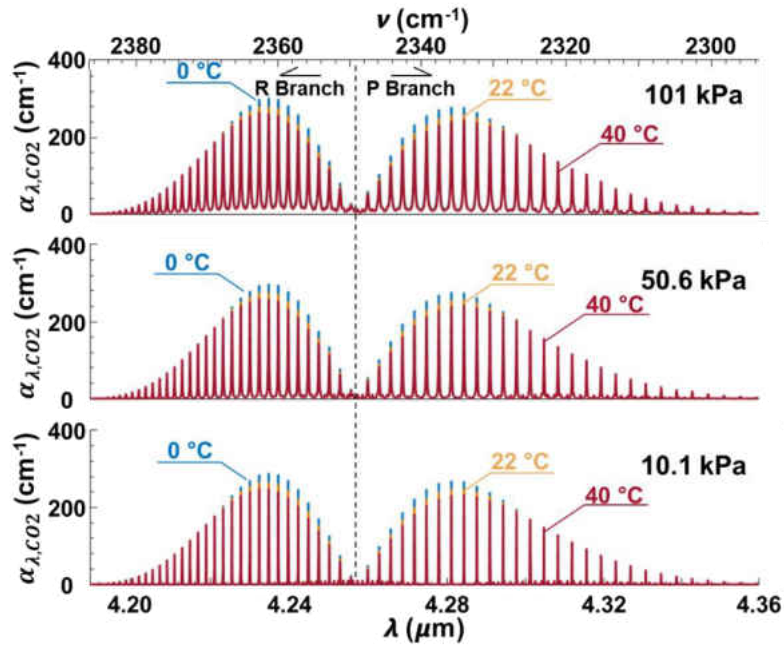
**Figure 6:** Absorption cross-section profiles for $CO_2$ at temperatures: 0˚C, 22 ˚C, 40 ˚C and pressures: 101 kPa, 50.6kPa, 10.1kPa [13].

The sensor optical schematic is seen in Figure 7 below. This follows the same general idea as the previous optical design, but the reduction to one species of interest and correspondingly one test LED meant that the test path length could be increased while staying within the payload's size constraints. This design change also greatly reduced power requirements.
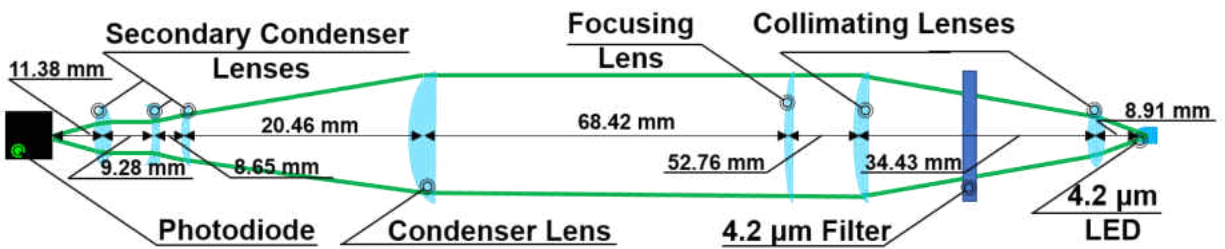


**Figure 7:** Sensor optical path for the high-altitude balloon flight [14].

Figure 8 below shows a model of the acrylic enclosure that was designed to house the electronic and optical components as well as the plate used to attach the sensor to the HASP

balloon gondola. This acrylic enclosure ultimately also had ribbed fins placed around the outside for further protection and for assisting with heat dissipation. Passthroughs were created in the acrylic walls for necessary power and signal cables. Further thermal management was provided for the LED with the aid of solid copper heat sinks.
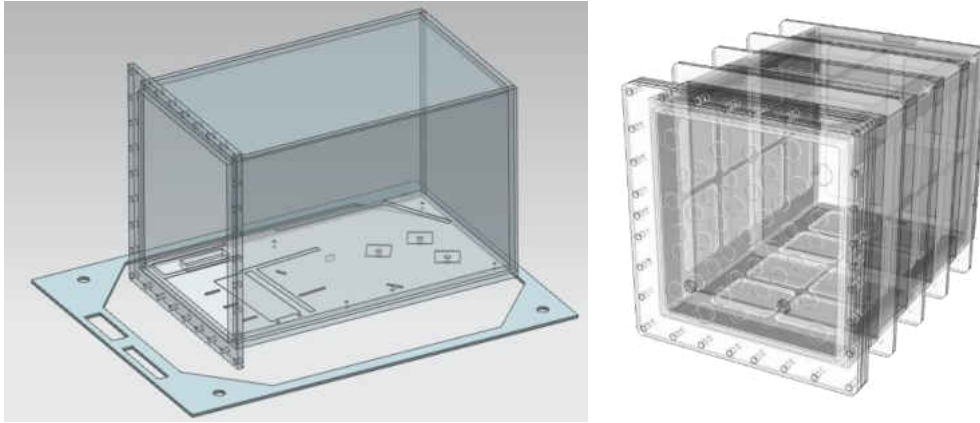


**Figure 8:** Model of the acrylic enclosure for the sensor placed on top of the HASP plate [14].

The sensor's electrical schematic is shown in Figure 9. The payload was provided with 30VDC from the HASP gondola during the flight. This voltage had to be stepped down for the various electrical components, as can be seen in part (B) of the figure. The cRIO Data Acquisition Unit (DAQ) (National Instruments) and the solenoid valve relay required 24VDC, while a 12VDC line was setup to power the photodiode. Three separate 5VDC lines were used to power the state-variable circuit, the LED driver circuit, and the amplifier circuit. The LED driver circuit was designed as an open-loop system and contained a ceramic capacitor to allow for temperature-dependent frequency changes. In this manner, the effects of the temperature changes could be more clearly monitored.
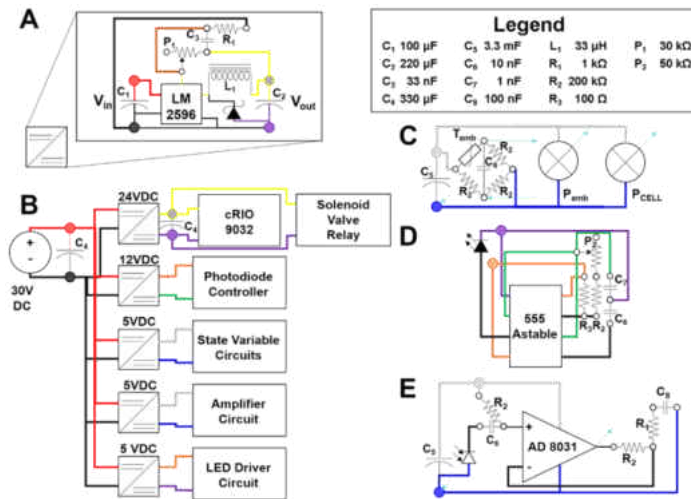
**Figure 9:** Sensor electrical schematic [13]. (A) DC/DC converter; (B) Power distribution network. Source power provided by HASP gondola; (C) State variable circuit; (D) LED driver circuit; (E) Photodiode amplifier circuit.

## *Flight Test and Results*

Figure 10A shows the aluminum housing that went over the acrylic enclosure. This housing was also used to physically attach the sensor to the HASP plate. The housing was designed for both physical protection and to provide additional heat dissipation by being spray-painted white. Figure 10B shows the enclosure positioned on the flight gondola, as it was undergoing ground testing prior to the balloon launch.
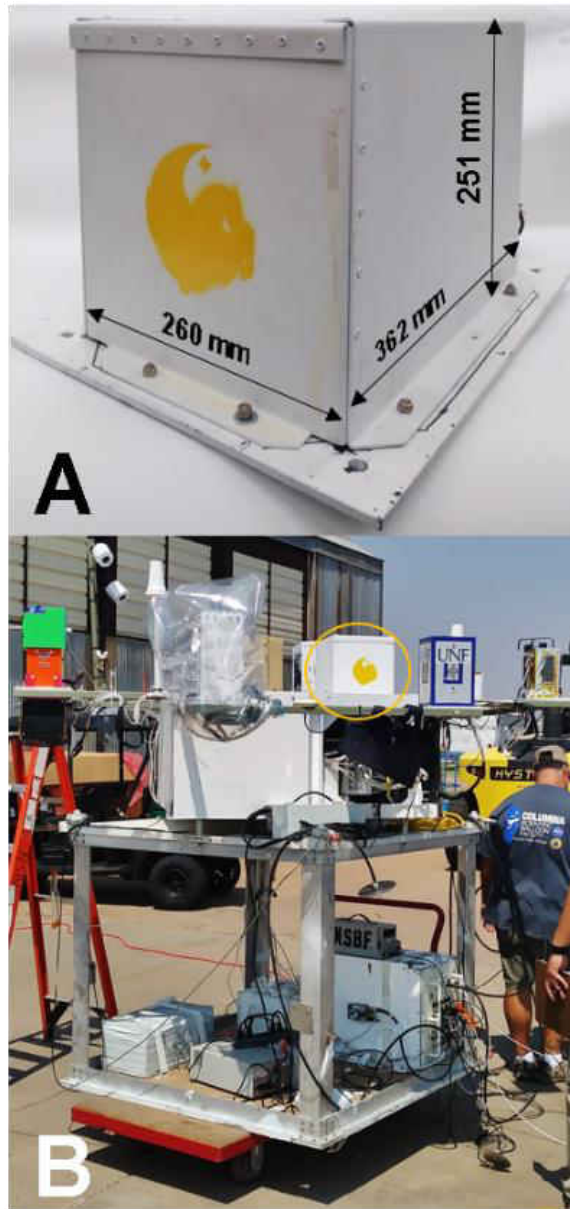
**Figure 10:** (A) Sensor mounted to the HASP platform; (B) Sensor on the HASP gondola prior to balloon launch [13].

The balloon flight occurred at the NASA Columbia Scientific Balloon Facility at Ft. Sumner, New Mexico. The entire flight lasted for a total of approximately 13 hours, and float was reached at 138 minutes into the flight. This was designed to be an autonomous operation test, so the data was recorded onto the DAQ and was analyzed after retrieving the system. The enclosure was sealed with ambient air while on the ground. Figure 11 shows the effect of enclosure

temperature on the signal frequency. Here, $F_{max}$ *(kHz)* represents the *locus of frequency*, or the LED's modulation frequency. $A_{max}$ *(mV·Hz)* represents the *integral quantity of the collected signal along the frequency axis at fixed time steps*.
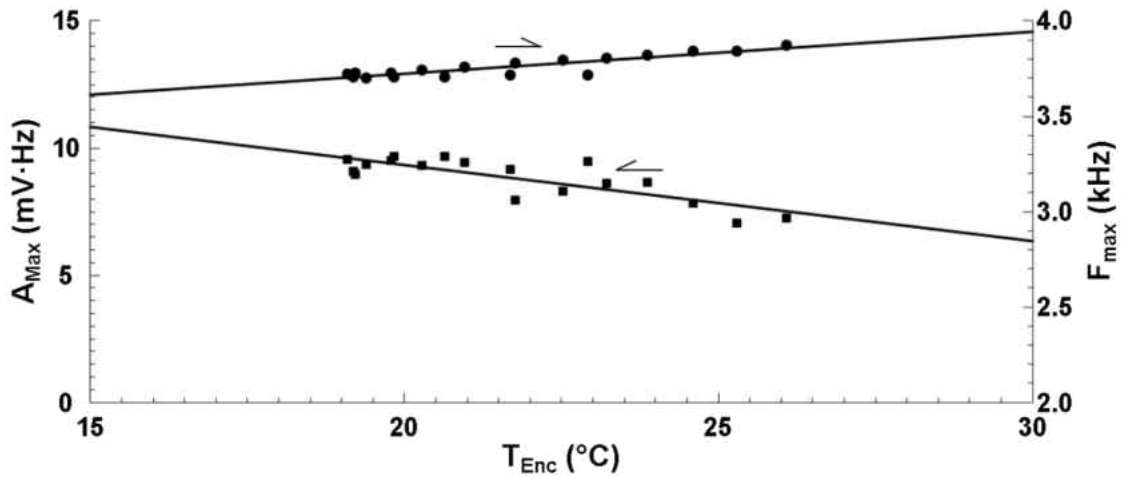


**Figure 11:** $A_{max}$ and $F_{max}$ as functions of enclosure temperature during the high-altitude balloon flight [13].

# CHAPTER FOUR: ROTATING GRATING DESIGN

## Overview

The sensor described here is the most recent iteration of the LED-based hazardous gas detector. It used a reflective grating, as explained in Chapter Two, to diffract light from a single LED source such that multiple species may be detected; this grating was paired with an exit slit to ensure proper wavelength selection. The species of interest are $CO_2$ and $N_2O$. The switch from CO to $N_2O$ was made partly because of the LED's (Thorlabs LED4300P) spectral output, as shown in Figure 12. Since $N_2O$ is closer to the center wavelength than CO, better results could be achieved for it. Additionally, $N_2O$ is still a hazardous gas that must have its concentration closely monitored in space environments.
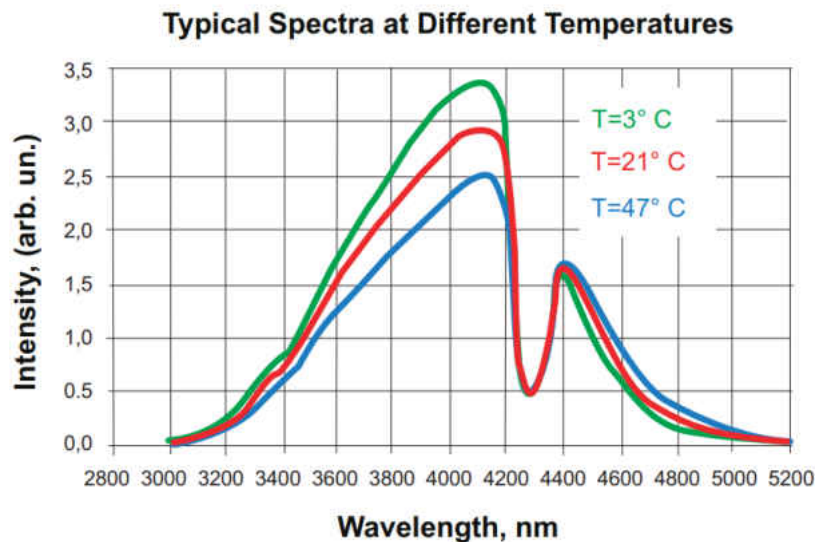


**Figure 12:** Spectral output with respect to wavelength for LED4300P (Thorlabs) [16].

Figure 12 also demonstrates the effect of temperature on the relative intensity of the LED. It can be seen that output intensity increases as temperature is reduced, until a point of approximately 4300 nm; after this, the intensity decreases as temperature is reduced.

The sensor schematic for the rotating grating design can be seen in Figure 13 below. Light leaves the source LED and is collimated before passing through a test cell containing the species of interest. The test cell has an internal path length of 14cm. The attenuated light then reaches the grating and is chromatically dispersed such that a relatively monochromatic diffracted wavelength reaches the condenser lenses and exit slit before being focused onto the detector. The slit was opened to a span of ±0.98mm during testing, which means that a range of ±5.061nm from the intended centerline wavelength was allowed to reach the detector. A function generator (BK Precision, 4005DDS) was used to modulate the LED at a constant frequency of 250 kHz [11, 12]. No additional load matching was employed in this setup, partly in order to keep power usage minimal. A manual rotating stage mount (Newport, TR80) was used in this setup, and it allowed for 360 degrees of coarse rotation and 6 degrees of fine rotation; this limit of 6 degrees of fine rotation was taken into account when determining the optimal setup location of the LED and detector in order to record the wavelength range of interest. A stepper motor (Lin Engineering) was attached to the fine rotation knob and controlled via an Arduino Uno. The Arduino code checked for signals from the USB-6366 Data Acquisition Unit (DAQ) (National Instruments) in order to discern when the experiment is occurring and whether to move forwards or backwards.
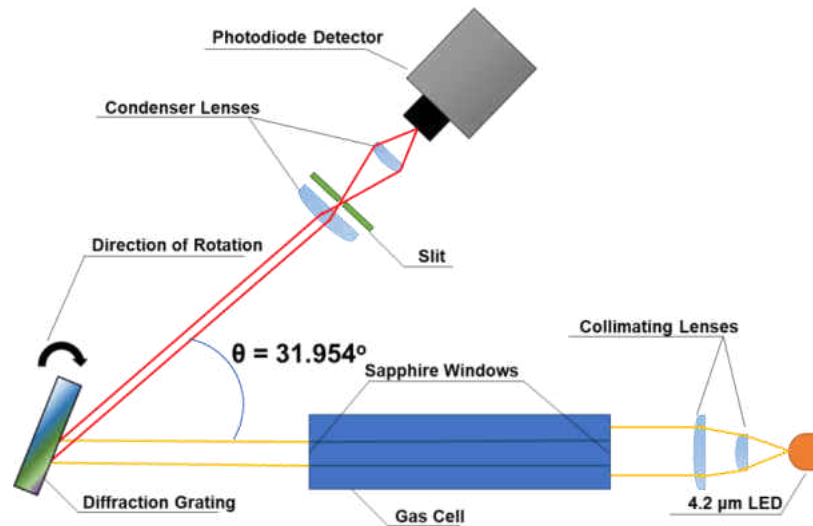
**Figure 13:** Sensor schematic showing how light from the LED traverses the optical path via the rotating grating.

Figure 14 below shows a simplified diagram of the LabVIEW code used to control the experiment. The Arduino was controlled by the DAQ in order to ensure that data would only be collected while the grating was stationary. The Arduino also controlled a thermistor which was used to measure and record the environmental temperature at each step. The saved data includes the signal from the detector, the input signal from the function generator, and the environmental temperature.
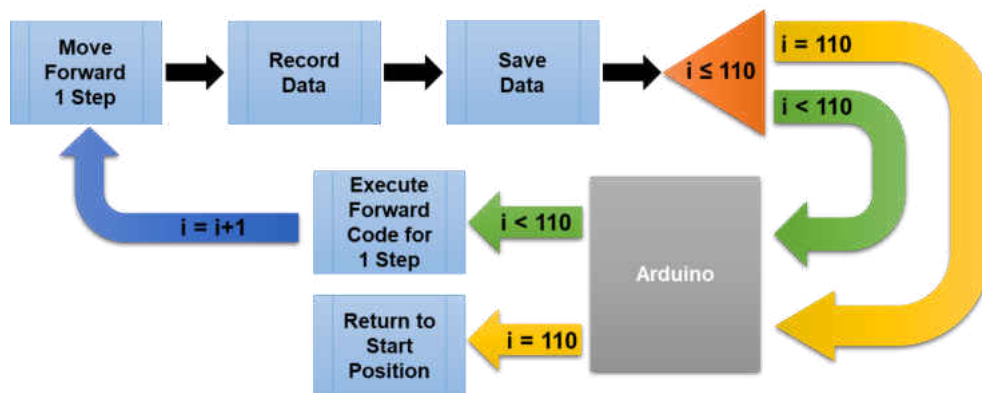


**Figure 14:** DAQ programming logic diagram.

Calibration

It is important to calibrate the system prior to testing so that there is no question as to what is being measured. Since the grating rotated a set amount for each experiment, the starting position, the amount of moment for each step, and the total rotation amount (and corresponding wavelength range) must remain constant.

Optical calibration to determine the exact locations of the detector and LED with respect to the grating was performed with the use of a laser diode centered at 650 nm. Figure 15 below depicts the general procedure involved in calculating the reference angle labeled as $\theta$. The laser was positioned as seen in the figure. The grating was then rotated so that it was both vertically and horizontally aligned with the laser, such that the incident light was reflected back to its source; this was confirmed by measuring the distance between diffraction modes on a flat surface with a Vernier Caliper (Capri Tools, 20140428). After the angle on the rotating stage was noted for this starting position, the grating was rotated until a mode passed through the gas cell and reached the LED. Given the order of the node and the angle of rotation, $\varphi_1$, Equation 3 was used to determine the angle between the laser and the LED; in this situation, $\varphi$ is equal to $\alpha + \beta$. The grating was then further rotated such that the same mode passed through the optical slit and reached the detector, and the new angle $\varphi_2$ was used to determine the angle between the detector and the laser. Thus, ultimately, the reference angle between the LED and the detector could be determined. This process was completed several times and an average value of $\theta = 31.954^\circ$ was determined for use in experimentation.
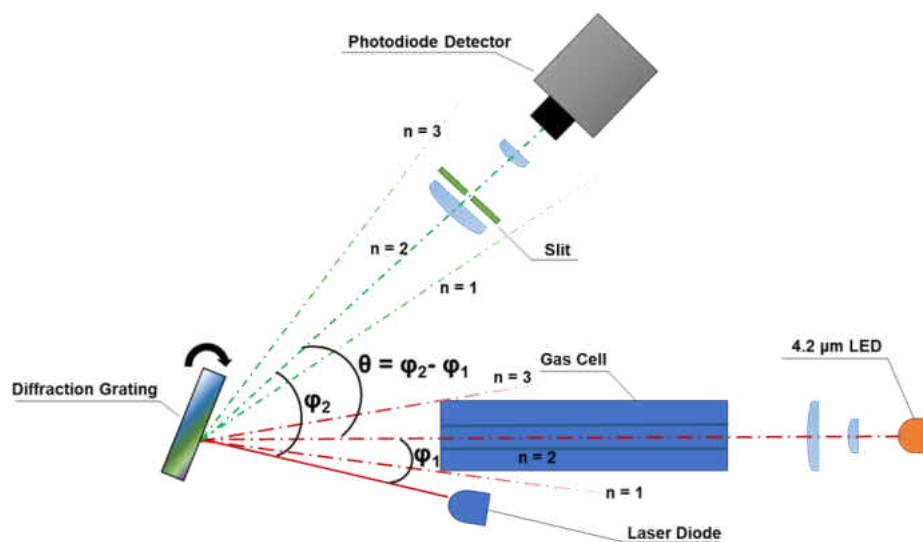
**Figure 15**: Optical calibration setup procedure. Modes that are not of interest for the calculations are shown to be gradually fading.

Manual calibration involved ensuring that the step size and total range of rotation both remained constant. Step size was controlled through the Arduino's programming, while the total range was decided in the DAQ's visual interface. The main source of any drift was determined to be the attachment of the stepper motor to the rotation stage's fine tuner. This was resolved by attaching the stepper motor onto the grating itself, such that the motor also rotated as the grating rotated; Figure 16 displays a picture depicting this setup. Several full-scale tests were then performed, in which the grating rotated for the total range and returned to its original position. Once these tests could be completed approximately 20 times with no deviation between start position and final position, any drift present was deemed negligible.
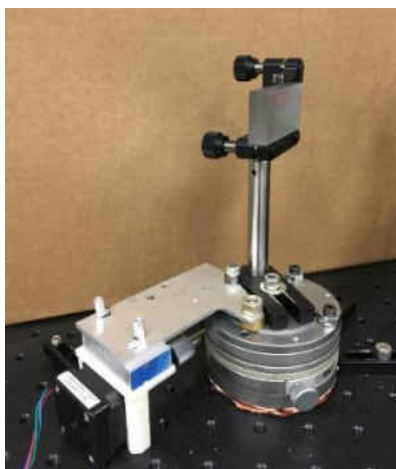
**Figure 16:** Stepper motor attached to the grating's rotation stage.

<u>Data Collection</u>

The total range for tests was determined to be 110 total steps, where the Arduino instructs the stepper motor to rotate $23.4°$ at each step. This resulted in a total rotation angle of $5.8°$ and a wavelength range of 4117 nm to 4592nm. The setup was placed in a laboratory fume hood in order to maintain a controlled environment and minimize exposure to any potential leaks from the test cell. A vacuum calibration test was taken, in which the test cell was vacuumed to 0.48 Torr, in order to serve as the reference intensity in the experimental absorbance calculations as shown in Equation 1.

All tested mixtures contained some concentration of $CO_2$ and $N_2O$ balanced in nitrogen ($N_2$). Prior to testing the actual mixtures, separate interference tests were performed; one test contained only $CO_2$ balanced in $N_2$ and the other contained only $N_2O$ balanced in $N_2$. The mixtures were prepared by filling a lecture bottle with the concentrations listed in Table 1 below. A total of three separate mixtures were prepared for the experiment, and subsequent tests at varying concentrations were performed by filling the test cell with a certain amount of $N_2$ before adding

22

the test mixture. Mixtures were prepared in a manifold with the use of a pressure transducer (MKS Baratron, ±0.25%). Each test was completed 3-4 separate times in order to examine repeatability.

**Table 1:** Mixture Concentration Values

| Mixture | Percentage of $CO_2$ (%) | Percentage of $N_2O$ (%) | Percentage of $N_2$ (%) |
|---------|--------------------------|--------------------------|-------------------------|
| 1 | 0.778 | 0.774 | 98.5 |
| 2 | 0.548 | 0.551 | 98.9 |
| 3 | 0.355 | 0.356 | 99.3 |

## Discussion of Results

Because the data recorded by the DAQ was saved in terms of Decibels (dB), it must first be converted to a linear intensity scale. This is done with the use of Equation 4 below [17]. Here, $P_2$ is the power being measured and $P_1$ is a reference value. $A$ represents the intensity in dB units. The power is kept in terms of this unitless ratio for further analysis since the reference power source theoretically remains constant for all values. However, since fluctuations in voltage do occur, the recorded function generator intensity value is used to normalize the absorbance calculations. Equation 1 is then used as planned in order to calculate absorbance.

$$\frac{P_2}{P_1} = 10^{\left(\frac{A}{10}\right)} \tag{4}$$

Figure 17 shows the calculated absorbance values for the cross-interference tests. The results show a minimal interference between the two locations when considering the peak wavelength. While interference is shown to exist near the 4400 nm area, further evaluation focuses on wavelength ranges for each species that do not overlap. This figure also shows a false baseline

absorbance, which appears even though voltage fluctuations were accounted for in the absorbance calculations. This is potentially due to the function generator slowly warming up and producing more voltage output as tests continue throughout the day. This false baseline is accounted for in further calculations by subtracting an average of the first few wavelengths in the testing range.
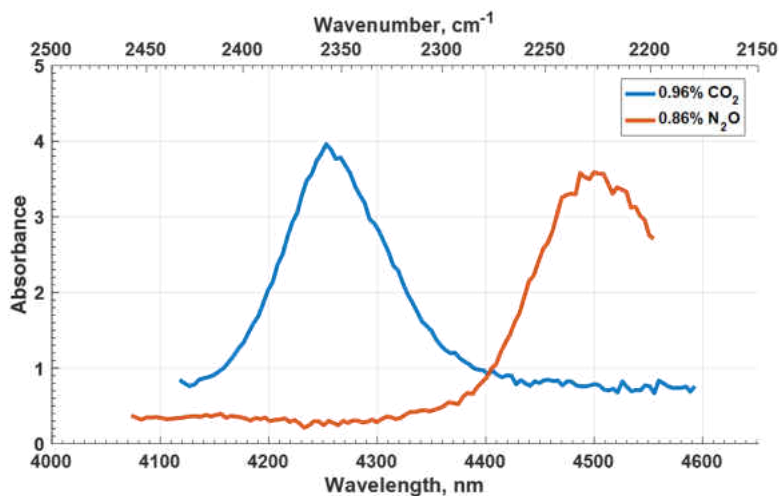


**Figure 17:** Calculated absorbance with respect to wavelength for the two cross-interference measurements. The first mixture contains 0.96% CO2 balanced in nitrogen and the second mixture contains 0.86% N2O balanced in nitrogen.

The experimental data is first linearly interpolated to approximately 40,000 points, and the theoretical absorption coefficient data is interpolated to the same length. Since the theoretical data is retrieved from HITRAN in terms of linearly increasing wavenumber and the experimental data is collected in terms of linearly increasing wavelength, the theoretical absorption coefficient data must also be converted to be in terms of linearly increasing wavelength.

### *Convolution of Spectra*

In order to accurately compare the experimental results with theoretical predictions, the absorption coefficient must be convolved with the instrument function. However, since the setup is not easily categorized as a pre-built spectrometer, the convolution is instead determined by

comparing the theoretical absorbance curve with the experimental until the half-widths are approximately equal. Ultimately, a Gaussian apparatus function with a half-width of 35 cm$^{-1}$ is determined for use in further calculations. The convolution was performed using the downloaded absorption coefficient data and a specifically designed MATLAB function. The same convolution function is used to smooth the experimental absorbance data with a half-width of 3 cm$^{-1}$ [18]. The theoretical data is then further smoothed by the same amount in order to keep comparison consistent.

*Integrated Absorbance Calculations*

The integrated absorbance is calculated for a certain wavelength range for both $CO_2$ and $N_2O$ separately, and it is then divided by the number of points in that range. Figure 18 below shows the integrated absorbance calculations for $CO_2$ while Figure 19 shows the integrated absorbance calculations for $N_2O$. All theoretical predictions are shown in black. The data is separated by mixture number in order to be able to compare across mixtures as well. The $CO_2$ data is taken from a wavelength range of 4150 nm – 4350 nm, while the $N_2O$ data is taken from a wavelength range of 4420 nm – 4585 nm. The error bars shown on each point depict the standard deviation for each concentration value.
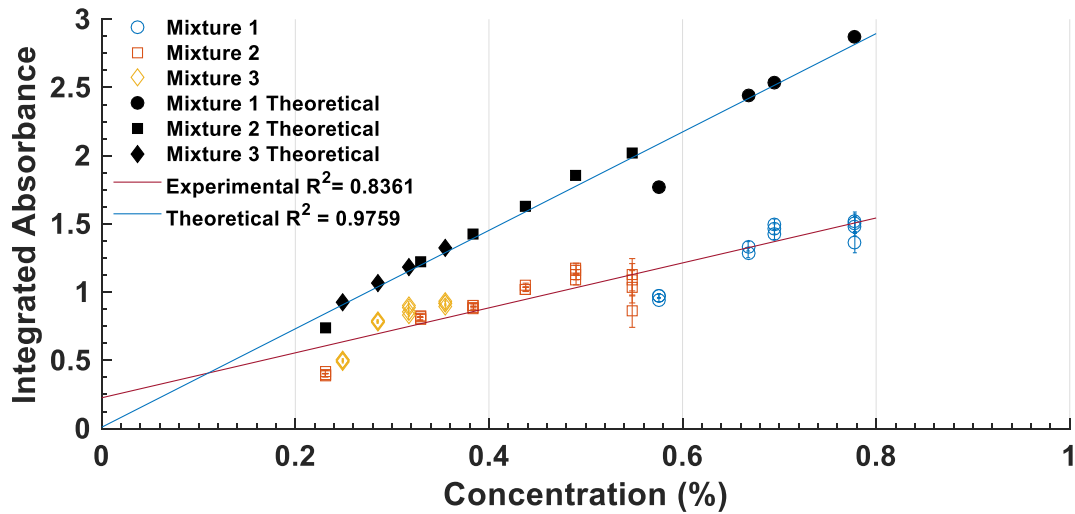
**Figure 18:** Integrated absorbance values for $CO_2$ for all data points. The black markings show the theoretical predictions based on HITRAN data and the colorful points show the experimental data separated by mixture number.
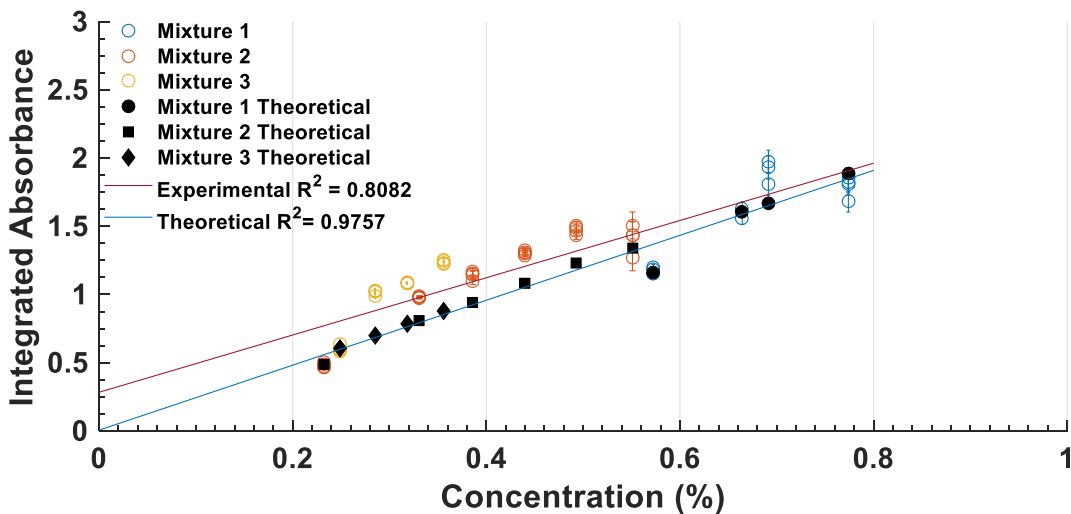


**Figure 19:** Integrated absorbance values for $N_2O$ for all data points. The black markings show the theoretical predictions based on HITRAN data and the colorful points show the experimental data separated by mixture number.

Based on the figures above, the experimental results follow the same general trend as the experimental results. On the whole, the $N_2O$ data better matches the theoretical predictions than the $CO_2$ data. The $CO_2$ data also matches the prediction better at lower concentrations and

integrated absorbance values. Linear trendlines are used to approximate the data and match extremely well for the theoretical calculations. The trendlines appear to diverge as concentration increases for $CO_2$ but converge or correlate better as concentration increases for $N_2O$.

*Laser Validation*

Validation for this setup was performed with the use of two Distributed Feedback Quantum Cascade Lasers (QCL) (Thorlabs, QD4250CM1AS), (Thorlabs, QD4580CM1). The first laser has a wavelength range of $4.256 – 4.266\mu m$ and is used to measure $CO_2$; the second has a wavelength range of $4.583 – 4.596\mu m$ and is used to measure $N_2O$ in this experiment [19]. The general setup for the lasers is seen in Figure 20 below. The output of the laser diagram is transmitted to the existing grating design setup with the use of a fiber-optic coupler; this coupler's end location replaces the LED's position in Figure 14. Another fiber-optic coupler is used to send the same laser signal to a spectrum analyzer (Bristol, 771B) so that any drift that occurs during testing could be monitored. It is not possible in this situation for both wavelengths to diffract from the grating and reach the detector in a combined state; the grating is first rotated such that the $CO_2$ laser will reach the detector and then further rotated such that the $N_2O$ laser will reach the detector.
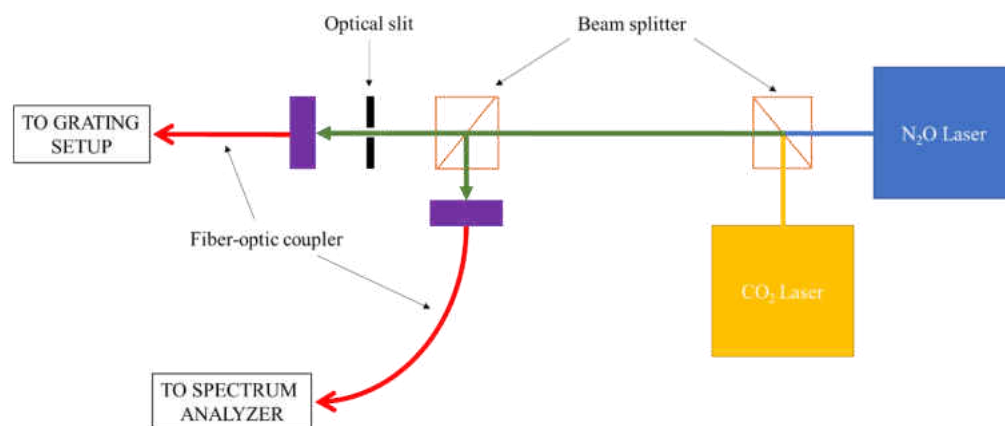


**Figure 20:** Laser setup diagram. The signal from both lasers is combined via a beam splitter and transmitted to both the grating setup and to a spectrum analyzer via another beam splitter and fiber-optic couplers.

27

Table 2 below shows the validation mixtures used during testing. The mixtures were prepared in the same manner as those used for the LED-based experiments.

**Table 2:** Laser Validation Mixture Concentrations

| Mixture | Percentage of $CO_2$ (%) | Percentage of $N_2O$ (%) | Percentage of $N_2$ (%) |
|---------|--------------------------|--------------------------|-------------------------|
| 1 | 0.355 | 0.356 | 99.29 |
| 2 | 0.674 | 0.654 | 98.67 |
| 3 | 0.518 | 0.503 | 98.97 |
| 4 | 0.537 | 0.521 | 98.94 |
| 5 | 0.201 | 0.195 | 99.60 |

Figures 21 and 22 below compare the calculated concentration data from the laser experiments with similarly calculated concentration data from the LED experiments; the first figure shows the results for $CO_2$ and the second shows the results for $N_2O$. The concentration values are again calculated with the use of the Beer-Lambert Law (Equation 1). The LED's interpolated absorbance data is used to find the point at a matching wavelength with the laser output.
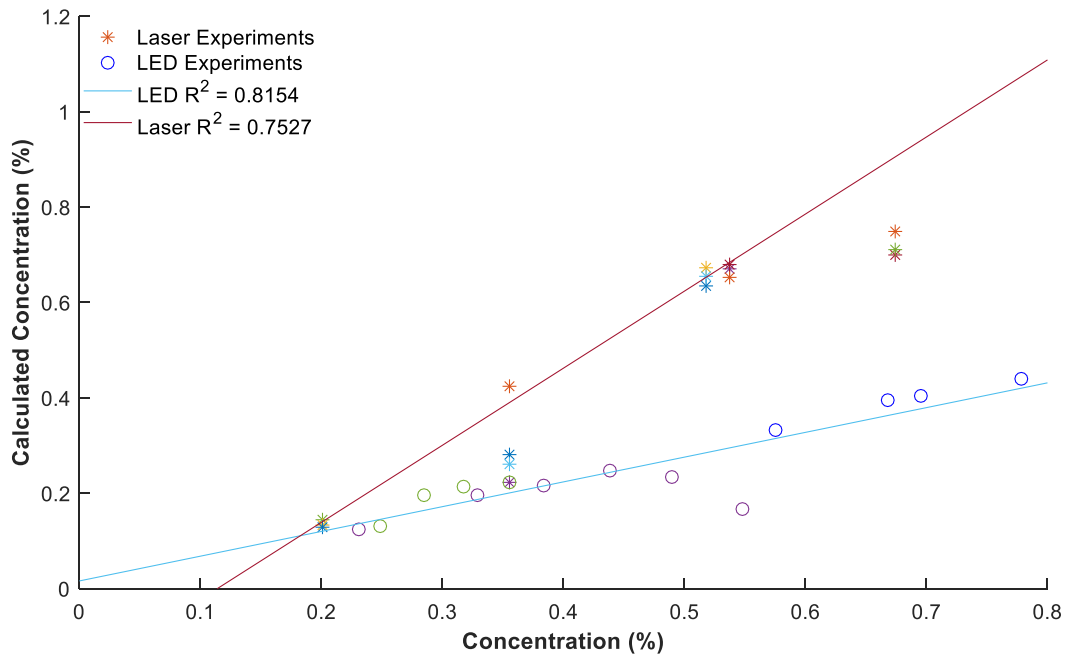
**Figure 21:** Laser and LED concentration calculations for $CO_2$ measurements. The mixture concentration is plotted on the x-axis, and the concentration calculated from intensity measurements is plotted on the y-axis.
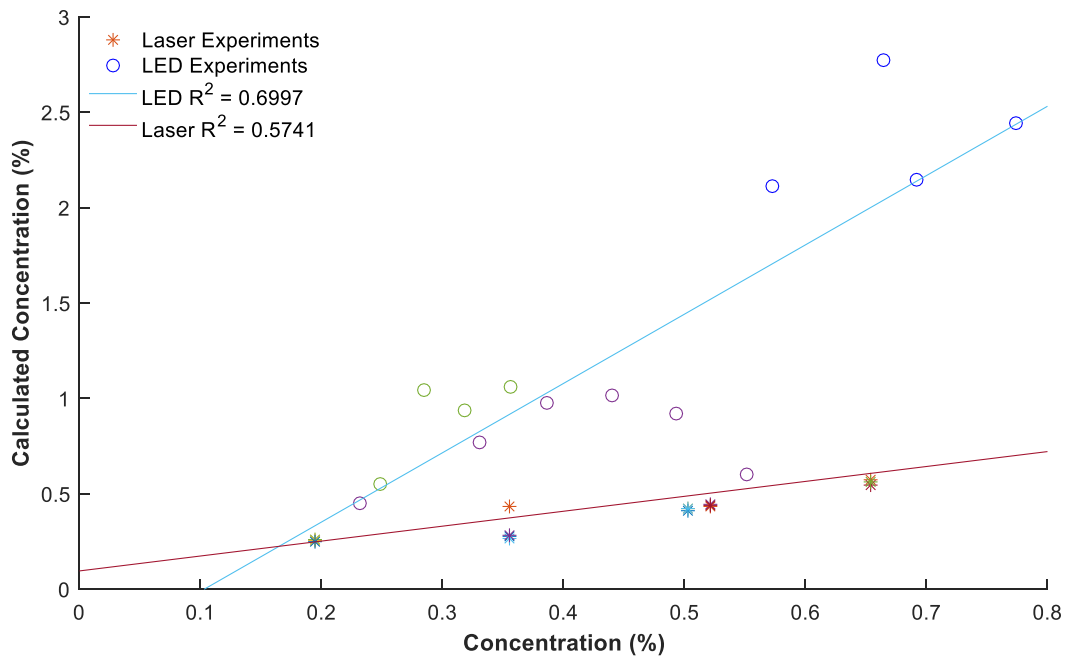


**Figure 22:** Laser and LED concentration calculations for $N_2O$ measurements. The mixture concentration is plotted on the x-axis, and the concentration calculated from intensity measurements is plotted on the y-axis.

From the two figures above, it is clear that the LED results correlate better with the laser results at lower concentrations. The method of looking at a single absorbance point for the LED and using this to calculate concentration  produces results with a poorer fit than by analyzing the integrated absorbance, especially with the $N_2O$ data. Another likely reason that the $CO_2$ data correlates better with the laser experiments than the $N_2O$ data is because the $CO_2$ laser, at 4264.314 nm, is spectrally closer to the peak of the expected LED absorbance curve. The laser used for $N_2O$ is lasing at 4589.6995 nm, which is spectrally located near the very end of the tested wavelength range. Not only is this position not the peak for the LED's $N_2O$ absorbance curve, the LED itself outputs at a lower intensity at this wavelength as seen in Figure 12.

# CHAPTER FIVE: CONCLUSIONS

Ultimately, an LED-based gas sensor has been tested in various configurations and environments in order to prove the technology's functionality as an early-warning hazardous gas and combustion detector. The design has been subjected to extreme changes in temperature and pressure as well as the physical stresses involved in a high-altitude balloon flight; its success in surviving these situations with minimal exterior damage proves the durability of the design. Additionally, the data collected from these tests show the effects of the environmental variables on absorbance measurements; these effects can be taken into account during any future environmental tests in order to improve sensor performance. The latest version of the sensor, the rotating grating version, has proved to be a functional method of using a single LED to detect multiple gases. The technique of scanning along a wavelength range and calculating the integrated absorbance means that wavelength drift is not a concern. While detection of the two species of interest does not occur simultaneously, the time required for a full-range sweep can be further optimized by better prioritizing wavelength subsets of interest. As this sensor technology improves further, the potential for it to replace existing sensors that are more fragile and expensive increases. In turn, as the costs associated for these basic safety measures decreases, the possibilities involved with commercial space travel will expand.

## Future Work

Future improvements for this design would focus on increasing the wavelength test range and decreasing the wavelength interval between the subsequent test points. The design can also be easily expanded to test for other gases, and the next gas to be added for single-LED based measurements would be CO; in this case, a cross-interference study between $N_2O$ and CO would

have to be performed. One of the major limitations of this design has been the lack of commercial availability of MIR LEDs with sufficient power ratings, but improvements have already been made in this field since the inception of this project. The design should also complete further hazardous environment tests in order to further prove its capabilities; in particular, microgravity testing would be essential. Another potential direction for future work is to use multiple LEDs with the single grating design in order to test for multiple gases simultaneously. The combined signal would be received by a single detector and separation of the various wavelengths could be achieved by modulation at different wavelengths, as was done previously with a multiple-LED setup.

# APPENDIX A: SPECIFICATION SHEETS FOR CRITICAL

# COMPONENTS

**THORLABS**

## LED with a Parabolic Reflector

**LED4300P**

## Description

The LED4300P emits light with a spectral output centered at 4200 nm. This LED is composed of heterostructures (HS) grown on a GaSb substrate. The diode is in a TO-18R Parabolic Reflector package.

## Specifications

It is recommended that this diode be used in a quasi-CW or pulsed regime (see diagram below). The operating temperature range is from -200℃ to 50℃.

Quasi-CW

Quasi-CW    f=2 kHz    200 mA    250 µs  250 µs

Pulsed

Pulse    1 µs    2 A    f=2 kHz    500 µs
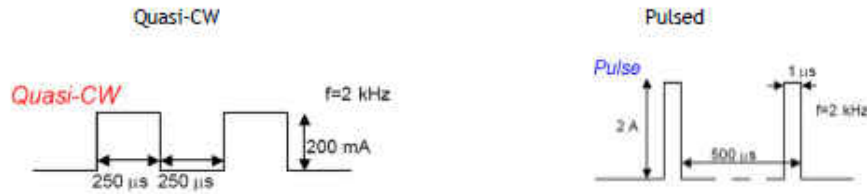
| Optical Specifications | |
| --- | --- |
| | Typical |
| Center Wavelength | 4200 nm ± 100 nm |
| FWHM | 900 nm |
| Optical Power (Minimum/Typical) @ 200 mA qCW | 0.01 mW |
| Optical Power Pulsed Mode @ 1A | 0.2 mW |
| Switching Time, ns | 30 ns |

| Soldering Specifications | |
| --- | --- |
| | Conditions |
| Manual Soldering | 295 ºC ± 5 ºC , for less than 3 seconds |
| Wave Soldering | 260 ºC ± 5 ºC , for less than 5 seconds |
| Reflow Soldering | **Preheating:** 70 ºC to 80 ºC , for 30 seconds<br>**Soldering:** 245 ºC ± 5 ºC , for less than 5 seconds |

May 2, 2011
22363-S01, Rev A

Specifications Subject to Change without Notice

34

## PVI-4TE Series

## 2 – 12 µm IR PHOTOVOLTAIC DETECTORS THERMOELECTRICALLY COOLED OPTICALLY IMMERSED
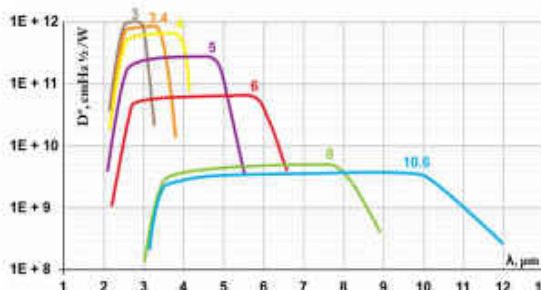


Example of D* vs Wavelength λ for PVI-4TE Series HgCdTe Detectors. Spectral Characteristics of individual detectors may vary from those shown on the chart.

### Features
- High performance in the 2 to 12 µm spectral range
- Fast response
- No flicker noise
- Convenient to use
- Wide dynamic range
- Compact, rugged and reliable
- Low cost
- Prompt delivery
- Custom design upon request

### Description

The **PVI-4TE-λ**opt photodetectors series (λopt - optimal wavelength in micrometers) feature four-stage thermoelectrical cooler IR phptpvoltaic detector, optically immersed to high refractive index GaAs hyperhemispherical (standard) or hemispherical or any intermediate lens (as option) for different acceptance angle and saturation level.

The devices are optimized for the maximum performance at λopt. Cut-on wavelength can be optimized upon request. Reverse bias may significantly increase speed of response and dynamic range. It results also in improved performance at high frequencies, but 1/f noise that appears in biased devices may reduce performance at low frequencies. Highest performance and stability are achieved by application of variable gap **HgCdTe** semiconductor, optimized doping and sophisticated surface processing. Custom devices with quadrant cells, multielement arrays, different windows, lenses and optical filters are available upon request.

Standard detectors are available in **TO8** packages with **wAl2O3** or **wZnSeAR** windows. Other packages, windows and connectors are also available.

### IR Detector Specification @20°C

| Parameter | Symbol | Unit | PVI-4TE-3 | PVI-4TE-3.4 | PVI-4TE-4 | PVI-4TE-5 | PVI-4TE-6 | PVI-4TE-8 | PVI-4TE-10.6 |
|---|---|---|---|---|---|---|---|---|---|
| Optimal Wavelength[1] | $\lambda_{opt}$ | µm | 3 | 3.4 | 4 | 5 | 6 | 8 | 10.6 |
| Detectivity[1]: @ $\lambda_{peak}$ @ $\lambda_{opt}$ | D* | $\frac{cm \cdot \sqrt{Hz}}{W}$ | $\geq 1.0 \times 10^{12}$ $\geq 8.0 \times 10^{11}$ | $\geq 8.0 \times 10^{11}$ $\geq 7.0 \times 10^{11}$ | $\geq 6.0 \times 10^{11}$ $\geq 4.0 \times 10^{11}$ | $\geq 3.0 \times 10^{11}$ $\geq 1.0 \times 10^{11}$ | $\geq 6.0 \times 10^{10}$ $\geq 4.0 \times 10^{10}$ | $\geq 5.0 \times 10^{9}$ $\geq 4.0 \times 10^{9}$ | $\geq 4.0 \times 10^{9}$ $\geq 2.0 \times 10^{9}$ |
| Current Responsivity | $R_i$ | $\frac{A}{W}$ | ≥0.5 | ≥0.8 | ≥1 | ≥1.3 | ≥1.5 | ≥1.5 | ≥0.7 |
| Time Constant | τ | ns | ≤280 | ≤200 | ≤100 | ≤80 | ≤50 | ≤30 | ≤10 |
| Time Constant[1] | τ | ns | ≤3 | ≤2 | ≤1 | ≤0.7 | ≤0.5 | ≤0.4 | ≤0.4 |
| Resistance – Optical Area Product | R·A | $\Omega \cdot cm^2$ | ≥30000 | ≥2000 | ≥800 | ≥40 | ≥3 | ≥0.06 | ≥0.05 |
| Operating Temperature | T | K | ~195 | | | | | | |
| Acceptance Angle, F/# | Φ, - | deg, - | 36, 1.62 | | | | | | |

[1] Other Optimal Wavelengths available upon request.
[1] Data sheet states minimum guaranteed D* values for each detector model. Higher performance detectors can be provided upon request.
[1] Response which may be achieved at reverse bias (selected detectors upon request). Devices with faster response are available upon special request.

| Type | Optical Area[1] [mm×mm] | | | | | | | | | |
|---|---|---|---|---|---|---|---|---|---|---|
| | 0.025×0.025 | 0.05×0.05 | 0.1×0.1 | 0.2×0.2 | 0.25×0.25 | 0.5×0.5 | 1×1 | 2×2 | 3×3 | 4×4 |
| PVI-4TE-3 | | | | | O | X | X | O | | |
| PVI-4TE-3.4 | | | | | O | X | X | O | | |
| PVI-4TE-4 | | | | | O | X | X | O | | |
| PVI-4TE-5 | | | | | O | X | X | O | | |
| PVI-4TE-6 | | | | | O | X | X | | | |
| PVI-4TE-8 | | | | | | X | X[1] | P | | |
| PVI-4TE-10.6 | | | | | | X | X[1] | P | | |

[1] Circular shaped Optical Area (Diameter [mm]) can be provided upon request.
[1] Custom detectors may require reverse bias in order to increase Dynamic Resistance to improve frequency response.
X – standard detectors
P – default with reverse bias
O – detectors available upon request; parameters may vary from these in Data Sheet

# REFERENCES

1. Excellence, C.o. *COE CST RESEARCH STRUCTURE*. Center of Excellence - Commercial Space Transportation; Available from: http://www.coe-cst.org/researchstructure.html.

2. Chandler, F., Ambrose, R., Biegel, B., Brown, T., Carter, J., Culbert, C., Edwards, C., Fox, J., Glaessgen, E., Hurlbert, K., Israel, D., Johnson, L., Kliss, M., Linne, D., Meador, M., Mercer, C., Meyer, M., Motil, B., Munk, M., Nesnas, I., Prince, J., Ryan, R., Scott, J., and Siochi, E. *2015 NASA Technology Roadmaps*. NASA 2015; Available from: http://www.nasa.gov/offices/oct/home/roadmaps/index.html.

3. Satish, U., et al., *Is CO2 an indoor pollutant? Direct effects of low-to-moderate CO2 concentrations on human decision-making performance.* Environmental health perspectives, 2012. **120**(12): p. 1671.

4. Nickels, L., *Memories of spaceshipone.* Reinforced Plastics, 2017. **61**(2): p. 83-86.

5. Rothman, L.S., et al., *The HITRAN2012 molecular spectroscopic database.* Journal of Quantitative Spectroscopy and Radiative Transfer, 2013. **130**: p. 4-50.

6. Friedman, R., *Risks and issues in fire safety on the space station.* 1993.

7. Teichert, H., T. Fernholz, and V. Ebert, *Simultaneous in situ measurement of CO, H 2 O, and gas temperatures in a full-sized coal-fired power plant by near-infrared diode lasers.* Applied Optics, 2003. **42**(12): p. 2043-2051.

8. Vurgaftman, I., J. Meyer, and L. Ram-Mohan, *High-power/low-threshold type-II interband cascade mid-IR laser-design and modeling.* IEEE Photonics Technology Letters, 1997. **9**(2): p. 170-172.

9. Piatt, U. and J. Stutz, *Differential Optical Absorption Spectroscopy, Principles and Applications.* 2008, Springer, Heidelberg.

10. Palmer, C.A. and E.G. Loewen, *Diffraction grating handbook.* 2005: Newport Corporation New York.

11. Thurmond, K., et al., *A light-emitting diode-(LED-) based absorption sensor for simultaneous detection of carbon monoxide and carbon dioxide.* Applied spectroscopy, 2016. **70**(6): p. 962-971.

12. Villar, M.S., et al., *High-Altitude Balloon Flight Demonstration of LED-Based NDIR Multi-Gas Sensor for Space Applications*, in *AIAA SPACE and Astronautics Forum and Exposition*. 2017, American Institute of Aeronautics and Astronautics.

13.     Terracciano, A., et al., *HAZARDOUS GAS DETECTION SENSOR USING BROADBAND LED BASED ABSORPTION SPECTROCOPY FOR SPACE APPLICATIONS.* New Space, 2018. **Article in press**.

14.     Terracciano, A. and A. Parupalli, *Hazardous Gases for Harsh Environments LED Sensor*, in *HASP Final Flight Report 2017*. 2017.

15.     Rothman, L., et al., *The HITRAN database: 2012 edition.* J Quant Spectrosc Radiat Transfer, 2013.

16.     Thorlabs. *LED4300P - 4200 nm LED with Parabolic Reflector, 10 µW Quasi-CW, 200 µW Pulsed, TO-18R* Available from: https://www.thorlabs.com/thorproduct.cfm?partnumber=LED4300P.

17.     mogami.com. *dB Conversion*. Available from: www.mogami.com/e/cad/db.html.

18.     Kranendonk, L.A., A.W. Caswell, and S.T. Sanders, *Robust method for calculating temperature, pressure, and absorber mole fraction from broadband spectra.* Applied optics, 2007. **46**(19): p. 4117-4124.

19.     Thorlabs. *Quantum Cascade Lasers (QCLs)*. Available from: https://www.thorlabs.com/newgrouppage9.cfm?objectgroup_id=6932.